

# Revealing compact structures of interstellar plasma in the Galaxy with RadioAstron

E. N. Fadeev,<sup>1</sup> A. S. Andrianov,<sup>1</sup> M. S. Burgin,<sup>1</sup> M. V. Popov,<sup>1</sup> A. G. Rudnitskiy,<sup>1</sup>★  
V. I. Shishov,<sup>2</sup> T. V. Smirnova<sup>2</sup> and V. A. Zuga<sup>1</sup>

<sup>1</sup>*P. N. Lebedev Physical Institute, Astro Space Center, Profsoyuznaya 84/32, Moscow 117997, Russia*

<sup>2</sup>*P. N. Lebedev Physical Institute, Pushchino Radio Astronomy Observatory, Pushchino, Moscow Region 142290, Russia*

Accepted 2018 July 20. Received 2018 July 19; in original form 2018 March 16

## ABSTRACT

The aim of our work was to study the spatial structure of inhomogeneities in the interstellar plasma in the directions of five pulsars: B0823+26, B0834+06, B1237+25, B1929+10 and B2016+28. Observations of these pulsars were made with the RadioAstron space–ground radio interferometer at 324 MHz. We measured the angular size of the scattering discs and found it to be in the range 0.63–2.1 mas. We determined the position of scattering screens on the line of sight. Independent estimates of the distances to the screens were made from the curvature of parabolic arcs revealed in the secondary spectra of four pulsars. Based on the results, we came to the conclusion that scattering is produced mainly by compact plasma layers and the uniform model of inhomogeneity distribution along the line of sight is not applicable.

**Key words:** scattering – techniques: high angular resolution – pulsars: general – ISM: general – radio continuum: ISM.

## 1 INTRODUCTION

The radio emission from cosmic sources propagating through the interstellar medium (ISM) is distorted by turbulent inhomogeneous plasma. It is subject to dispersion and scattering. The study of scattering effects makes it possible to investigate the structure of inhomogeneities in interstellar plasma and to reveal effects that distort the initial properties of radiating objects.

The most efficient way to study these effects is to observe scintillations of the radio emission from pulsars, since they are point sources and the results of the analysis are not distorted by the influence of the intrinsic structure of the emission region. Extensive theoretical and experimental studies of scattering effects started to be carried out all over the world immediately after the discovery of pulsars in 1967 (Armstrong, Rickett & Spangler 1995; Shishov & Smirnova 2002; Scheuer 1968; Rickett 1977, 1990; Gwinn, Bartel & Cordes 1993; Gwinn et al. 1998; Stinebring et al. 2001). However, there are many unsolved problems in this field.

On 2011 July 11, the *Spektr-R* spacecraft, with a 10-m radio telescope on board, was launched from Baikonur cosmodrome to a high-apogee orbit. The space radio telescope, together with the largest ground radio telescopes, formed the RadioAstron space–ground interferometer. The space observatory operates at four radio wavebands: 92, 18, 6 and 1.35 cm (Kardashev et al. 2013; Kovalev et al. 2014).

One of the scientific research fields of the RadioAstron project is probing the interstellar plasma using radio pulsars. The RadioAstron interferometer provides great advantages in the study of scattering effects, since it makes it possible to measure directly the angular size of the scattering discs that are usually enclosed in the interval from 0.01–0.001 arcsec at decimetre wavelengths. For ground interferometers, such scattering discs are usually unresolved.

Our goal was to investigate the distribution of scattering material along the lines of sight to five pulsars using dynamic and secondary spectra analysis. We present the results of investigation of the structure of inhomogeneities in the interstellar plasma toward five pulsars: B0823+26, B0834+06, B1237+25, B1929+10 and B2016+28. Section 2 of this article explains the features of the data processing (calibration and normalization) and describes the parameters of the observations used for analysis; Section 3 defines the basic concepts and functions used in the analysis. Sections 4 and 5 present specific results for each pulsar and the final two sections present a discussion and conclusion.

## 2 OBSERVATIONS AND DATA REDUCTION

The dates and duration of the observations were chosen in such a way that projection of space–ground baselines increased from values of the order of the Earth’s diameter to values at which the scattering disc was completely resolved. Due to thermal constraints for the space radio telescope (SRT), the duration of space–ground observations was limited to 1–2 hrs. Data were transmitted from RadioAstron in real time to Pushchino or Green Bank tracking station,

★ E-mail: [almax1024@gmail.com](mailto:almax1024@gmail.com)

where they were recorded using the RadioAstron Data Recorder (RDR).

The space radio telescope used one-bit quantization and the ground telescopes two-bit quantization for signal digitizing. All observations presented in this article were conducted at 324 MHz. The signal was recorded in two polarization channels (RCP, LCP). The SRT and ground telescopes were recording one frequency sub-band: 316–332 MHz.

Each observation consists of separate segments (scans) with a duration of 570 s and technical pause of 30 s between them. Correlation of all observations presented was performed with the Astro Space Center (ASC) Correlator (Likhachev et al. 2017) using the on-pulse gating mode and incoherent dedispersion. The integration time for each pulsar pulse was set equal to the pulse width at 10 per cent of its magnitude. Correlation for OFF-pulse data was performed with the same gate parameters, in order to determine amplification variations within the sub-band for further calibrations of ON-pulse data, as well as to calculate normalization parameters for visibility functions.

The correlator output consists of complex cross-spectra calculated for each pulsar period and averaged by the single pulse duration ON-pulse and OFF-pulse. The number of spectral channels  $N_{\text{ch}}$  was set according to the decorrelation bandwidth values  $f_{\text{dif}}$ , determined in our previous studies.

Dynamic spectra are used to estimate the scintillation time  $t_{\text{dif}}$ . Additional averaging of complex cross-spectra was performed for the case in which the scintillation time was significantly larger than the pulsar period. The number of frequency channels and integration times of the spectra are given in Table 1.

The dynamic auto or cross spectrum  $I(f_i, t_j)$  is a two-dimensional discrete complex function of frequency  $f_i$  and time  $t_j$ , where  $i \in [0; N_{\text{ch}} - 1]$  is the number of spectral channels and  $j \in [0; N_{\text{pulses}} - 1]$  the number of pulses. For most tasks, a cross-spectra module is used:  $F(f_i, t_j) = \sqrt{\Re(I(f_i, t_j))^2 + \Im(I(f_i, t_j))^2}$ .

Additionally, a bandpass correction was applied for each telescope. We calculated an average autospectrum (module)  $\langle F(f_i) \rangle$  of OFF-pulse data for each scan (570 s) and then retrieved the bandpass characteristics  $B(f_i)$ . As a result, the analysed function was

$$F_{\text{norm}}^{ab}(f_i, t_j) = \frac{F_{\text{ON}}^{ab}(f_i, t_j) - F_{\text{OFF}}^{ab}(f_i, t_j)}{\sqrt{B^a(f_i)B^b(f_i)}}, \quad (1)$$

where  $F_{\text{ON}}^{ab}(f_i, t_j)$  and  $F_{\text{OFF}}^{ab}(f_i, t_j)$  are the modules of cross spectra between antennas ‘a’ and ‘b’ for ON-pulse and OFF-pulse;  $B^a(f_i)$  and  $B^b(f_i)$  are the bandpass characteristics for the corresponding antennas. Strong interference was removed individually by replacing the affected frequencies by random values with an average and dispersion determined from the neighbouring portion of the spectrum. Examples of such dynamic spectra are shown in Fig. 1. Then we calculated the two-dimensional correlation functions of the dynamic spectra:

$$DCCF(\Delta f_n, \Delta t_m) = \frac{\sum_{i=0}^{N_{\text{ch}}-1} \sum_{j=0}^{N_{\text{pulses}}-1} F_{ij} F_{i+n, j+m}}{(N_{\text{ch}} - n)(N_{\text{pulses}} - m)}, \quad (2)$$

where  $n \in [-N_{\text{ch}}/2 + 1; N_{\text{ch}}/2 - 1]$  and  $m \in [-N_{\text{pulses}}/2 + 1; N_{\text{pulses}}/2 - 1]$ .

To determine  $f_{\text{dif}}$  and  $t_{\text{dif}}$ , we used cross-sections of two-dimensional correlation functions in frequency  $DCCF(\Delta f_n, 0)$  and time  $DCCF(0, \Delta t_m)$ . For  $f_{\text{dif}}$  we took the half-width of the central component at half maximum in  $DCCF(\Delta f_n, 0)$  and for  $t_{\text{dif}}$  we took the half-width  $DCCF(0, \Delta t_m)$  of the central component at  $1/e$  level.

As was shown in Shishov et al. (2003), time and frequency structure functions for small lags  $\Delta t$  and  $\Delta f$  can be obtained from the correlation function of intensity fluctuations. This was used in the article.

The pulsed nature of pulsar emission and the relatively high flux density of individual pulses make it possible to measure the increments of the signal in the correlation gate directly. Thus a simple normalization relationship can be used. The visibility function  $V^{ab}$  is divided by the normalization factor:

$$R_{\text{norm}} = \sqrt{(V_{\text{ON}}^a - V_{\text{OFF}}^a)(V_{\text{ON}}^b - V_{\text{OFF}}^b)}, \quad (3)$$

where  $V_{\text{ON}}^a$ ,  $V_{\text{OFF}}^a$ ,  $V_{\text{ON}}^b$  and  $V_{\text{OFF}}^b$  are the visibility amplitudes obtained from autospectra in ON-pulse and OFF-pulse gates respectively. These values are, in fact, equivalent to the signal standard deviation. Due to the low sensitivity of the space radio telescope ‘b’ compared with the ground stations, the value  $V_{\text{ON}}^b - V_{\text{OFF}}^b$  is determined with significantly lower accuracy. Therefore we need to use a different expression to calculate the normalization factor for space–ground baselines:

$$R_{\text{norm}} = (V_{\text{ON}}^a - V_{\text{OFF}}^a) \sqrt{\eta V_{\text{OFF}}^b / V_{\text{OFF}}^a}, \quad (4)$$

where  $\eta$  is the ratio between the equivalent system flux density (SEFD) of the ground radio telescope (GRT) and the space radio telescope (SRT):  $\eta = SEFD_{\text{GRT}} / SEFD_{\text{SRT}}$ .

Finally, the frequency covariation function  $J(\mathbf{b}, \Delta f)$  of complex cross-spectra is obtained by summing individual correlation functions for strong pulses in the complex form. The ratio of the modulus level of this function outside the decorrelation bandwidth to its maximum value at zero frequency lag is related to the normalized amplitude of the visibility function for a given interferometric baseline via (8).

### 3 BASIC RELATIONS

The two-dimensional Fourier transform of the dynamic spectrum  $I(f, t)$  is the secondary spectrum of the pulsar  $S_I(\tau, \nu)$ , where  $\tau$  is delay and  $\nu$  is fringe frequency.

Stinebring et al. (2001) showed that parabolic structures ( $\tau \propto \nu^2$ ) are observed in the secondary spectra of many nearby pulsars and these are caused by the presence of scattering screens. The curvature  $a$  is related to the distance to the scattering screen from the observer, as follows (Stinebring et al. 2001):

$$a = \frac{D\lambda^2}{2c|V_{\text{eff}}|^2} \frac{1-s}{s}, \quad (5)$$

where  $\lambda$  is the wavelength of observations,  $c$  the speed of light,  $s = (D - d_s)/D$ , where  $D$  is the distance to the pulsar and  $d_s$  the distance from the observer to the screen, and  $V_{\text{eff}}$  the velocity of the diffraction pattern in the observer plane. This velocity is determined as a geometrical sum of the pulsar velocity components  $V_{\text{psr}}$ , observer’s velocity  $V_{\text{obs}}$  and scattering screen velocity  $V_{\text{scr}}$  perpendicular to the line of sight:

$$V_{\text{eff}} = \frac{d_s}{D - d_s} V_{\text{psr}} + V_{\text{obs}} - \frac{D}{D - d_s} V_{\text{scr}}. \quad (6)$$

Usually the pulsar velocity is greater than the observer’s velocity and the expected screen velocity. As a result, we neglect these velocity components. Thus it is possible to estimate the distance to the scattering screens by measuring the curvature  $a$  of parabolic structures in the secondary spectrum.

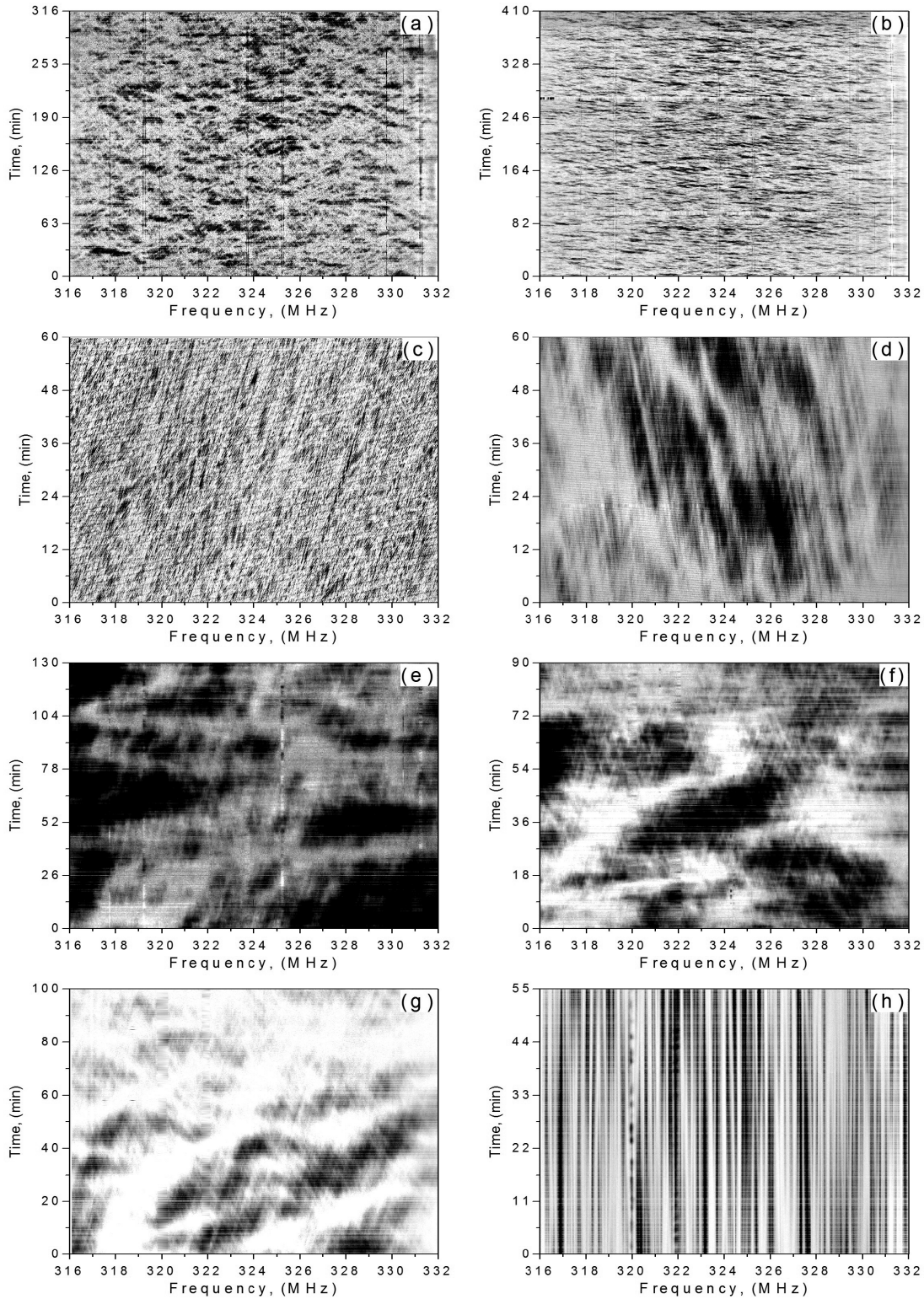


**Figure 1.** Dynamic spectra for observed pulsars: (a) B0823+26 (observation RAGS04AJ, 2015 March 11, GBT radio telescope), (b) B0823+26 (observation RAGS04AK, 2015 March 11, GBT radio telescope), (c) B0834+06 (observation RAES06C, 2012 April 26, Arecibo radio telescope), (d) B0834+06 (observation RAGS04AH, 2014 December 8, GBT radio telescope), (e) B1237+25 (observation RAGS04AP, 2015 May 13, GBT radio telescope), (f) B1237+25 (observation RAGS04AR, 2015 June 7, Arecibo radio telescope), (g) B1929+10 (observation RAGS04AO, 2015 May 5, Arecibo radio telescope), (h) B2016+28 (observation RAGS04AQ, 2015 May 22, Arecibo radio telescope).

For the regime of strong scintillations (Shishov et al. 2017),

$$J(\mathbf{b}, \Delta f) = |B_u(\Delta f)|^2 + |B_u(\mathbf{b})|^2, \quad (7)$$

where  $|B_u(\Delta f)|^2$  is the covariation function of flux fluctuations, which does not depend on the interferometer baseline projection,  $\Delta f$  is the frequency lag and  $B_u(\mathbf{b})$  the spatial function of field coherence (average flux equal to unity). For  $\Delta f = 0$ , we have  $J(\mathbf{b}, \Delta f = 0) = 1 + |B_u(\mathbf{b})|^2$ ; for frequency lags exceeding the diffraction scale,  $\Delta f > f_{\text{dif}}$ , we have  $J(\mathbf{b}, \Delta f > f_{\text{dif}}) = |B_u(\mathbf{b})|^2$ . Accordingly, the normalized covariation function is

$$\frac{J(\mathbf{b}, \Delta f > f_{\text{dif}})}{J(\mathbf{b}, \Delta f = 0)} = \frac{|B_u(\mathbf{b})|^2}{1 + |B_u(\mathbf{b})|^2}, \quad (8)$$

where the value  $|B_u(\mathbf{b})|$  can be estimated from the dynamic spectrum analysis. Note that for an unresolved source (ground-based interferometer)  $|B_u(\mathbf{b})| = 1$ ; if  $|B_u(\mathbf{b})| < 1$ , then the source is resolved and it is possible to estimate the spatial scale of the scattering disc:

$$B_u(\mathbf{b}) = \exp \left[ -\frac{1}{2} \left( \frac{|\mathbf{b}|}{\rho_{\text{dif}}} \right)^\alpha \right], \quad \alpha = n - 2. \quad (9)$$

Here  $n$  is the turbulence spectral index and  $\rho_{\text{dif}}$  the field coherence scale in the observer's plane. The spatial scale is related to the time-scale as

$$\rho_{\text{dif}} = |\mathbf{V}_{\text{eff}}| t_{\text{dif}}, \quad (10)$$

where  $\mathbf{V}_{\text{eff}}$  is determined by (6). We estimate  $\rho_{\text{dif}}$  and use the following relation to obtain the radius of the scattering disc:

$$\theta_{\text{sc}} = \lambda (2\pi\rho_{\text{dif}})^{-1}. \quad (11)$$

Note that here  $\theta_{\text{sc}}$  is the disc radius.

We also estimated the scattering disc size from the distribution of visibility amplitude versus baseline projections using the following fitting function (Gwinn et al. 1993):

$$V_{ab} = V_0 \exp \left[ -\frac{1}{2} \left( \frac{\pi}{\sqrt{2 \ln 2}} \frac{\theta_{\text{H}} b}{\lambda} \right)^\alpha \right], \quad (12)$$

where  $\theta_{\text{H}}$  is the angular diameter of the scattering disc, defined as the full width of the equivalent Gaussian at half magnitude. The amplitude of the visibility function was determined from the secondary spectra at time intervals less than the scintillation time. The visibility amplitude was estimated as the maximum value of the visibility function, which is usually located at delay and fringe frequency lags that are close to zero. Note that  $\theta_{\text{H}} = 2\sqrt{2 \ln 2} \cdot \theta_{\text{sc}}$ . We measured  $\theta_{\text{H}}$  by two methods: (1) by calculating covariation functions (using equations 8, 9 and 11) and (2) by approximating the distribution of visibility amplitude versus baseline projection using (12). The method used is indicated in the section for the corresponding pulsar.

The temporal broadening or scattering time  $\tau_{\text{sc}}$  was measured by exponential approximation of the average visibility function obtained at the space–ground baseline:

$$V(\tau) = V_0 \exp(-\tau/\tau_{\text{sc}}) + C. \quad (13)$$

After calculating the scattering time  $\tau_{\text{sc}}$  and angular size of the scattering disc  $\theta_{\text{H}}$ , one can estimate the distance to the scattering screen (Britton, Gwinn & Ojeda 1998):

$$d_s = \left( \frac{\theta_{\text{H}}^2 D}{8c\tau_{\text{sc}} \ln 2} + 1 \right)^{-1} D. \quad (14)$$

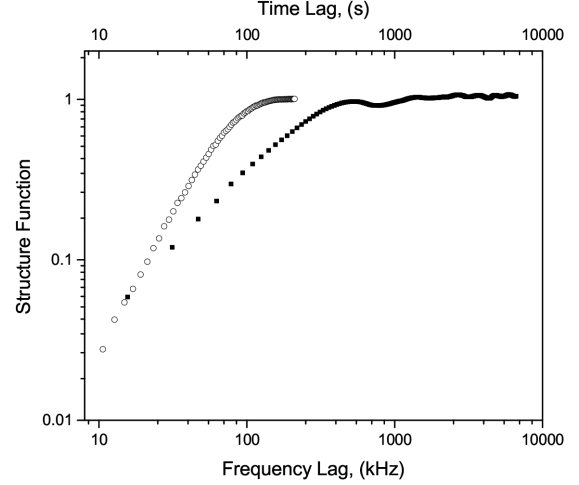


**Figure 2.** PSR B0823+26. Time (circles) and frequency (squares) structure functions.

## 4 RESULTS

### 4.1 Pulsar B0823+26

In observation RAGS04AK, most of the time the space–ground baselines were comparable or equal to the baseline projections between Green Bank and Westerbork telescopes. At the same time, the space radio telescope was located at its maximum distance from the Earth  $\approx 250\,000$  km. Observation RAGS04AJ was conducted 15 hrs earlier than RAGS04AK, when the baseline projection between the space radio telescope and Green Bank Telescope was five times larger than the Earth's diameter:  $b = 5.7 \times 10^9$  cm.

Parallax and proper motion were measured by Gwinn et al. (1986). The distance to the pulsar is 300–450 pc. In our measurements we used an average value of  $D = 360$  pc. The proper motion is  $\mu_\alpha = 62.6 \pm 2.4$  mas yr $^{-1}$ ,  $\mu_\delta = -95.3 \pm 2.4$  mas yr $^{-1}$ . For a distance of 360 pc, the pulsar tangential velocity is  $190 \pm 50$  km s $^{-1}$ . Fig. 1(a) and (b) shows the dynamic spectrum of the pulsar.

Spectra of individual pulses demonstrate fine structure, which is superimposed over an extended low-level component. Scintillation scales obtained from correlation analysis of dynamic spectra of both observations are  $f_{\text{dif}} = 140 \pm 5$  kHz and  $t_{\text{dif}} = 70 \pm 3$  s. Analysis of time and frequency structure functions showed that they have a power-law form, with power indices that differ by a factor of 2 (see Fig. 2). The index of the time structure function is  $\alpha = 1.65 \pm 0.02$  and, accordingly, the spectral index of plasma inhomogeneities fluctuations in the direction to the pulsar is close to Kolmogorov:  $n = \alpha + 2 = 3.65 \pm 0.02$ . Averaged over the session, the cross-correlation function (CCF) has a two-component structure: a main component with a scale of 140 kHz and a low-level broad component with a scale of about 1 MHz. With increasing time spacing between the spectra, these two components shift in frequency, with the relative amplitude of the low-level component becoming larger and its displacement stronger. It is possible that the two scales in the CCF are caused by anisotropy in the scattering media. It was shown in Rickett et al. (2014) that anisotropy can change the shape of the auto correlation function (ACF) significantly. To distinguish the shift more clearly, we have averaged the spectra over 20 pulsar periods.

Fig. 3 shows the shift of the CCF maximum in frequency, depending on the time lag between spectra. An approximation of this shift

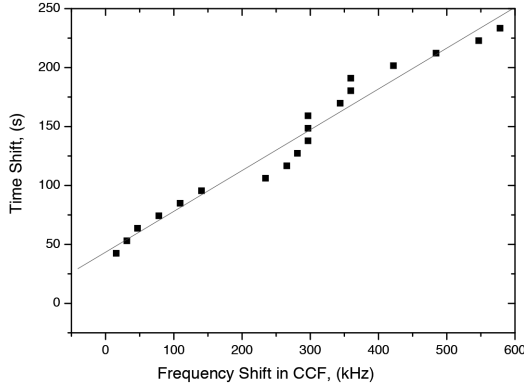


**Figure 3.** PSR B0823+26. Shift of CCF maximum with frequency ( $x$ -axis), depending on the time shift between spectra ( $y$ -axis), for the WB–GB baseline. The data are approximated with a linear function using the least-squares method:  $dt/df = 0.35 \pm 0.02 \text{ s kHz}^{-1}$ .

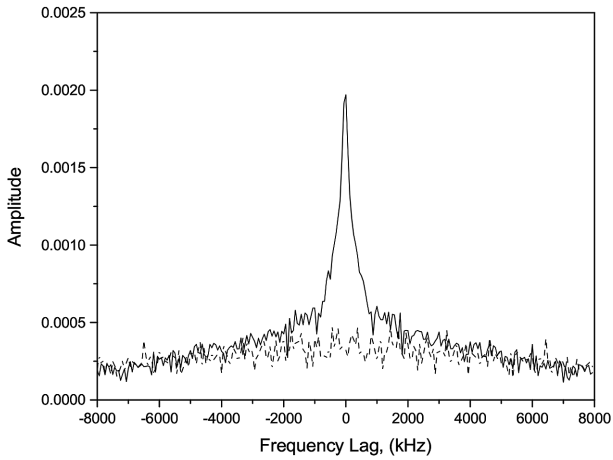


**Figure 4.** PSR B0823+26. Average covariation function of complex cross-spectra for space–ground baseline RadioAstron–Green Bank. The dashed line correspond to the OFF-pulse window.

is shown as a straight line. This shift corresponds to the shift of the narrow component. The shift of the broad component is difficult to measure, because of its low level and large width. The displacement of diffraction spots in the dynamic spectrum indicates the presence of refraction in the direction to the pulsar. The fact that the indices of the time and frequency structure functions differ by a factor of 2 indicates that the narrow component is dominated by diffraction effects (Shishov et al. 2003).

The spatial coherence function was obtained from analysis of the average covariation function of complex cross-spectra from the space–ground baseline RadioAstron–Green Bank (RA–GB, observation RAGS04AJ). This function is shown in Fig. 4 for ON-pulse and OFF-pulse signals, respectively. The extended envelope is caused by the residual influence of the receiver band. Using equation (8), we obtained the value of the spatial coherence function  $B_{\text{v}} = 0.45 \pm 0.05$ . The error here is defined as the sigma of variations in the tail of the covariation function. The normalized amplitude of the visibility function for space–ground baselines (small-baseline projections, large distance to the SRT) remained close to unity at  $0.84 \pm 0.05$ . In observation RAGS04AJ, conducted 15 hrs earlier,

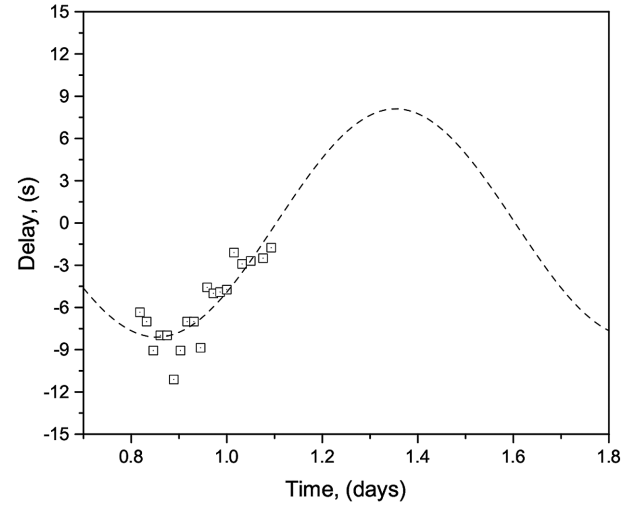


**Figure 5.** PSR B0823+26. Dependence of the scintillation pattern time lag between Westerbork and Green Bank ground telescopes on the time of day. Squares indicate the measured values; the dashed line corresponds to the approximation.

the amplitude of the visibility function was  $0.40 \pm 0.05$ , which coincides with the value of  $B_{\text{v}}$  obtained above.

The diffraction scale in the observer plane,  $\rho_{\text{dif}}$ , can be obtained using (9), taking  $\alpha = 1.65$  and  $b = 5.7 \times 10^9 \text{ cm}$ :  $\rho_{\text{dif}} = (4.3 \pm 0.4) \times 10^9 \text{ cm}$ . Using (10), one can estimate the distance from the observer to the scattering screen:  $d_s = 0.78D = 260 \text{ pc}$ . Here, we neglected the velocity of the observer and the screen, as these values are significantly smaller than the pulsar velocity. With (11), we determined  $\theta_{\text{sc}} = 0.76 \pm 0.09 \text{ mas}$ . Accordingly,  $\theta_{\text{H}} = 2.35\theta_{\text{sc}} = 1.8 \pm 0.2 \text{ mas}$ . The scattering time was estimated to be  $0.44 \pm 0.04 \mu\text{s}$  and using equation (14) we evaluated the distance to the screen as  $0.17 \pm 0.02 \text{ kpc}$ .

Observation RAGS04AK lasted for about 7 hrs. With such a long time interval, it was possible to trace the daily variation of scintillation pattern time delay between ground telescopes Westerbork and Green Bank. The maximum baseline between these telescopes was 4900 km as projected on to the proper motion vector. We have estimated the time lag of the scintillations between these telescopes by analysing the position of the maximum for a cross-section in time of the two-dimensional correlation function between the dynamic autospectra. The zero point is located well by the maximum of the narrow component in the cross-section corresponding to the intrinsic variability of the intensity of individual pulses. The position of the broad component maximum corresponding to scintillation distortions of the dynamic spectrum was determined by approximating the broad component with a Gaussian function (within the estimated scintillation time range).

In Fig. 5, squares show the dependence of the scintillation pattern time lag on the time of day. The dashed line corresponds to the approximation of observational data with a sinusoid function having a 24-hr period. The amplitude of the sinusoid was  $8.0 \pm 0.3 \text{ s}$ , which corresponds to a drift velocity of the scintillation pattern of  $610 \text{ km s}^{-1}$ . The intrinsic velocity of the pulsar determined from the measured proper motion is  $190 \text{ km s}^{-1}$ . Such a ratio between these velocities corresponds to the position of the scattering screen at a distance of  $(0.77 \pm 0.03)D$ . This estimate coincides with the distance to the scattering screen obtained above using a different method.

#### 4.2 Pulsar B0834+06

Three observations of B0834+06 were conducted on the following dates: 2012 April 26, 2014 December 8 and 2015 April 8. Ground telescopes participating in the observations, baseline projections and durations of sessions are shown in Table 1. The distance to the pulsar obtained from VLBI parallax measurements is (Liu et al. 2016)  $D = 0.62 \pm 0.06$  kpc. The pulsar proper motion is known with good accuracy (Lyne, Anderson & Salter 1982) and, for a given pulsar distance tangential velocity, is  $V_\alpha = 6 \pm 15$  km s<sup>-1</sup>,  $V_\delta = 151_{-18}^{+15}$  km s<sup>-1</sup>.

The number of frequency channels used for the correlation is given in Table 2. For the 2012 observation we used 65 536 channels, as in this session a finer structure of diffraction spots was observed. Fig. 1(c) and (d) shows dynamic spectra for two observations. Time and frequency scintillation scales obtained from these spectra are given in Table 3. A significant change in diffraction parameters occurred in 2012 April:  $f_{\text{dif}}$  decreased 50 times and  $t_{\text{dif}}$  nearly 20 times. In Bhat, Rao & Gupta (1999), scintillation parameters of 18 pulsars were monitored and, during the period 1993–1995, B0834+16 was observed 372 times over about 930 days. The average values of scintillation parameters were obtained in different series of observations:  $f_{\text{dif}}$  from 353–616 kHz and  $t_{\text{dif}}$  from 259–413 s, with root mean square error (RMS) of the order of 5 per cent for each value. Therefore, variations in the diffraction scale of a factor of tens, as observed in our study, constitute a rare event.

Dynamic spectra of observations conducted in 2014 and 2015 show clearly distinguishable inclined structures that indicate the presence of angular refraction in a given direction. Time and frequency structure functions obtained from analysis of the dynamic spectrum in 2015 showed their power-law character with an equal index of  $\alpha = 1.13 \pm 0.01$ , which corresponds to  $n = 3.13 \pm 0.01$ . The similarity of their inclinations indicates strong refraction in the direction to the pulsar. In the 2014 observation, we had a strong modulation in frequency and time, so a quality structure function could not be obtained. Such a modulation is well known as time and frequency ripples caused by the interference of diffracted and direct rays in dual-reflector radio telescopes. It was found that the diffracted rays from the sub-reflector edge can interfere with the main beam to produce a gain ripple of sinusoidal form for the dual reflector system. Analysis of the dynamic spectrum for 2012 gave the same slope of the structure functions,  $\alpha = 0.83 \pm 0.04$ .

For 2014 and 2015 observations, the drift of diffraction spots in the dynamic spectrum is clearly visible. In Bhat et al. (1999), it was noted that such drift behaviour is typical for this pulsar. Such a drift can last for quite a long time. This effect was observed during the entire series of observations conducted in 1993–1994 (110 days). This suggests that the structure leading to the refraction of radiation passes the line of sight for a time longer than 110 days.

Analysis of the complex covariation function module for the space–ground interferometer yielded the scale of the diffraction pattern. In Fig. 6, this function is shown for the 2015 observation for the RadioAstron–Arecibo (RA–AR) baseline. Applying equation (8), we found a value of the spatial coherence function  $B_u = 0.25 \pm 0.04$ . Using the values  $\alpha = 1.1$  and  $b = 1.52 \times 10^{10}$  cm, we obtained  $\rho_{\text{dif}} = (6.0 \pm 0.9) \times 10^9$  cm. The distance from the observer to the screen  $d_s$  was estimated using (10). Since the tangential velocity of the pulsar is  $V_{\text{psr}} = 151$  km s<sup>-1</sup>, we neglected the velocity of the Earth and the screen. Accordingly,  $d_s/D = 0.64 \pm 0.06$ ,  $d_s = 0.40 \pm 0.04$  kpc. Using (11), we calculated  $\theta_{\text{sc}} = 0.51$  mas,  $\theta_{\text{H}} = 1.2 \pm 0.4$  mas. We estimated the scattering time to be 0.76  $\mu$ s.

For 2014, we did not obtain a qualitative covariation function, because of the influence from frequency ripples. In the observation of 2012, the baseline projection of the space–ground interferometer was  $2.05 \times 10^{10}$  cm. For this day, we found the value  $B_u = 0.38 \pm 0.09$  and, using  $\alpha = 0.83$ , we determined the diffraction scale  $\rho_{\text{dif}} = (9.3 \pm 1.9) \times 10^9$  cm. From  $\rho_{\text{dif}}$ , we have  $\theta_{\text{H}} = 0.78 \pm 0.16$  mas. We obtained the value  $\tau_{\text{sc}} = 8 \pm 1$   $\mu$ s from exponential approximation of the average visibility function. Taking into account the scintillation time in this session,  $t_{\text{dif}} = 12 \pm 2$  s, and the pulsar velocity, we obtain  $d_s/D = 0.98$ . This means that the screen is located very close to the pulsar:  $d_s = 0.61 \pm 0.12$  kpc. Apparently there should be two scattering screens located along the line of sight; the screen that is closer to the pulsar is observed quite rarely. We will discuss the results obtained for B0834+06 in a separate article.

#### 4.3 Pulsar B1237+25

The parameters of two observations of this pulsar are shown in Tables 1 and 2. The shape of the interferometric fringes for the space–ground baseline indicates that the scattering disc for this pulsar was not resolved in these observations.

The scattering time was measured by an exponential approximation (13) of the averaged visibility functions obtained at space–ground baselines. For observation 13.05.2015, we found  $\tau_{\text{sc}} < 0.081 \pm 0.002$   $\mu$ s and for observation 07.06.2015  $\tau_{\text{sc}} < 0.114 \pm 0.003$   $\mu$ s. Errors in these measurements correspond to formal approximation errors. These estimates are comparable with the resolution of our observations and therefore were not used in the determination of the distance to the scattering screen.

The scintillation time  $t_{\text{dif}}$  and decorrelation bandwidth  $f_{\text{dif}}$  were measured from cross-sections of the two-dimensional autocorrelation function from dynamic spectra. For observation 13.05.2015, the scintillation time was  $t_{\text{dif}} = 209 \pm 1$  s and the decorrelation bandwidth  $f_{\text{dif}} = 526 \pm 18$  kHz, for observation 07.06.2015 we found  $t_{\text{dif}} = 285 \pm 5$  s and  $f_{\text{dif}} = 454 \pm 7$  kHz.

Structure functions in time and frequency for both observations have the same slope index:  $\alpha = 1.01 \pm 0.03$  and  $\beta = 1.04 \pm 0.02$  for observations 13.05.2015 and  $\alpha = 0.99 \pm 0.02$  and  $\beta = 1.00 \pm 0.02$  for observations 07.06.2015, respectively. This result indicates the refraction model of scintillation for this pulsar (Shishov et al. 2003; Smirnova & Shishov 2008).

Using (8), we have estimated the value  $B_u$  for the spatial coherence function for observation 13.05.2015:  $B_u = 0.87 \pm 0.11$ . Errors were determined as the sigma of variations in the tail of covariation function (8). These results lead to the conclusion that the scattering disc is not resolved.

#### 4.4 Pulsar B1929+10

The pulsar’s proper motion was measured by Kirsten et al. (2015):  $\mu_\alpha = 94.08 \pm 0.17$  mas yr<sup>-1</sup>,  $\mu_\delta = 43.25 \pm 0.16$  mas yr<sup>-1</sup>,  $D = 0.33 \pm 0.01$  kpc. The tangential velocity of the pulsar is  $V_{\text{psr}} = 177 \pm 6$  km s<sup>-1</sup>.

A 1.5-h observation was conducted on 2015 May 5. The baseline projection of the space–ground interferometer was 9.8 Earth diameters. Two ground radio telescopes participated in the observation: Westerbork and Arecibo. Interferometric fringes were detected for the space–ground baselines. The shape of these fringes indicates that the scattering disc for this pulsar was not resolved in these observations. The main scattering parameters, such as scintillation

**Table 1.** List of observations.

Pulsar	Obs. code	Epoch	Length of obs. (min)	Telescopes	Baseline projection (km)
B0823+26	RAGS04AJ	11.03.2015	316	GB	47 000–57 000
	RAGS04AK	11.03.2015	410	WB, GB	1000–20 000
B0834+06	RAES06C	26.04.2012	120	AR, EF	202 000–205 000
	RAGS04AH	08.12.2014	60	GB	63 000–64 000
	RAGS04AL	08.04.2015	95	AR, GB, WB	147 000–152 000
B1237+25	RAGS04AP	13.05.2015	130	GB	118 000–121 000
	RAGS04AR	07.06.2015	90	AR	78 000–80 000
B1929+10	RAGS04AO	05.05.2015	100	WB, AR	123 000–131 000
B2016+28	RAGS04AQ	22.05.2015	55	WB, AR	89 000–96 000

**Table 2.** Correlation parameters.

Pulsar	$D^1$ (kpc)	DM ( $\text{pc cm}^{-3}$ )	Averaging time	Spectral resolution
B0823+26	$0.36 \pm 0.08$	19.5	4P	1024/2048
B0834+06	$0.62 \pm 0.06$	12.9	4P	1024/65 536
B1237+25	$0.85 \pm 0.06$	9.25	P	512
B1929+10	$0.33 \pm 0.01$	3.18	P	512
B2016+28	$0.95 \pm 0.09$	14.2	4P	4096

Notes.  $D$  – distance to the pulsar,  $DM$  – dispersion measure,  $P$  – pulsar period.

(1) Distances were taken from parallax measurements (Gwinn et al. 1986; Briskin et al. 2002; Liu et al. 2016).

**Table 3.** Scattering parameters.

Pulsar	Obs. date	$f_{\text{dif}}$ (kHz)	$t_{\text{dif}}$ (s)	$\tau_{\text{sc}}$ ( $\mu\text{s}$ )	$\theta_{\text{H}}$ (mas)	$d_s$ (kpc)	$\rho_{\text{dif}}$ (km)	$n$
B0823+26	11.03.2015 (AJ) 11.03.2015 (AK)	$140 \pm 5$	$70 \pm 3$	$0.44 \pm 0.04$	$1.8 \pm 0.02$	$0.26 \pm 0.03$	$(4.3 \pm 0.04) \times 10^4$	$3.65 \pm 0.02$
B0834+06	26.04.2012 08.12.2014 08.04.2015	$4.0 \pm 0.05$ $350 \pm 20$ $210 \pm 10$	$12 \pm 2$ $314 \pm 10$ $220 \pm 15$	$8 \pm 1$ $0.76 \pm 0.09$	$0.78 \pm 0.16$ $1.2 \pm 0.4$	$0.61 \pm 0.12$ $0.40 \pm 0.04$	$(9.3 \pm 0.09) \times 10^4$ $(6.0 \pm 0.9) \times 10^4$	$2.83 \pm 0.04$ – $3.13 \pm 0.01$
B1237+25	13.05.2015 07.06.2015	$526 \pm 18$ $454 \pm 7$	$209 \pm 1$ $285 \pm 1$	$<0.081$ $<0.114$	$<0.8$ –	– –	$<1.7 \times 10^6$ –	$3.01 \pm 0.03$ $2.99 \pm 0.02$
B1929+10	05.05.2015	$619 \pm 5$	$233 \pm 1$	$<0.106$	$0.63 \pm 0.02$	$0.24 \pm 0.03$	$(1.1 \pm 0.02) \times 10^5$	$3.36 \pm 0.03$
B2016+28	22.05.2015	$43 \pm 2$	$2125 \pm 230$	$2.50 \pm 0.05$	$2.1 \pm 0.3$	$<0.1$	$(3.4 \pm 0.05) \times 10^4$	$3.05 \pm 0.02$

Note.  $f_{\text{dif}}$  – decorrelation bandwidth,  $t_{\text{dif}}$  – scintillation time,  $\tau_{\text{sc}}$  – scattering time,  $\theta_{\text{H}}$  – angular diameter of the scattering disc,  $d_s$  – distance to the scattering screen,  $\rho_{\text{dif}}$  – scale of diffraction pattern,  $n$  – spectral index of ISM inhomogeneities.

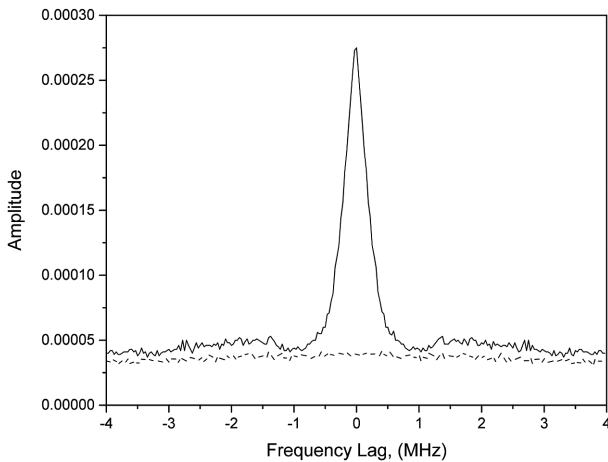


**Figure 6.** PSR B0834+06. Average covariation function from complex cross-spectra (observation 08.04.2015, baseline RadioAstron–Arecibo). The dashed line corresponds to the OFF-pulse window.

time, scattering time, decorrelation bandwidth, scattering disc size and distance to the scattering screen, were measured.

The scattering disc radius was calculated using two techniques. In the first case, the distribution of the amplitude of the visibility function versus the baseline was approximated by (12). In the second technique, the scattering disc radius was obtained from the field coherence scale. The scattering time is  $\tau_{\text{sc}} = 0.106(1) \mu\text{s}$ . The value of the measured scattering time is close to the time resolution ( $0.0625 \mu\text{s}$ ) and therefore can be taken as an upper limit. Scintillation scales are  $233 \pm 1 \text{ s}$  and  $619 \pm 5 \text{ kHz}$ . Errors in these measurements correspond to formal approximation errors. Previously measured values are  $350 \pm 20 \text{ s}$  and  $1200 \pm 80 \text{ kHz}$  (Bhat et al. 1999).

The scattering disc size  $\theta_{\text{H}}$  obtained from (12) is  $0.6(2) \text{ mas}$ . The high value of error is caused by the low number of ground-based telescopes participating in the observation.

The slope indices are  $\alpha = 1.36 \pm 0.03$  and  $\beta = 0.68 \pm 0.06$ . From (8), we obtained the spatial coherence function  $B_u = 0.56 \pm 0.04$  (Fig. 7). Using (9) and the index of the time structure function, we estimated a spatial coherence scale  $\rho_{\text{dif}} = (1.1 \pm 0.1) \times 10^5 \text{ km}$ . Therefore  $\theta_{\text{sc}} = 0.27 \pm 0.03 \text{ mas}$  and  $\theta_{\text{H}} = 0.63 \pm 0.06 \text{ mas}$ , which

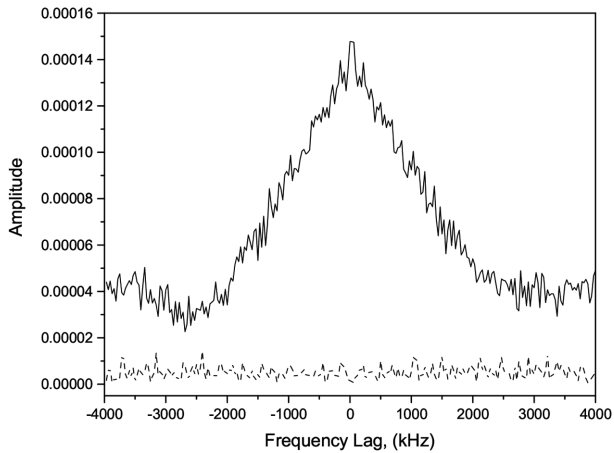


**Figure 7.** PSR B1929+10. Average covariation function from complex cross-spectra (observation 08.04.2015, baseline: RadioAstron–Arecibo). The dashed line corresponds to the OFF-pulse window.

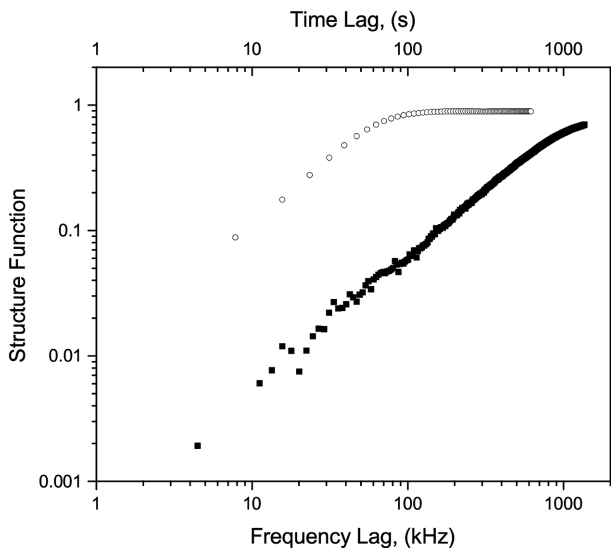


**Figure 8.** PSR B2016+28. Time (circles, top  $x$ -axis) and frequency structure function (squares, bottom  $x$ -axis) on a log–log scale.

coincides with previously obtained results. The distance to the scattering screen can be obtained using  $\rho_{\text{dif}}$  and  $t_{\text{dif}}$ . Neglecting the ISM velocity and the observer’s velocity, we obtain, using (10),  $d_s = 0.73D = 0.24 \pm 0.3$  kpc.

#### 4.5 Pulsar B2016+28

Observations were performed on 2015 May 22 at 324 MHz with a space–ground baseline projection of about 92 000 km, with the Arecibo radio telescope as a ground segment. The dynamic spectrum for this pulsar is shown in Fig. 1(h).

Correlation analysis of the dynamic spectrum yielded scintillation frequency and time-scales  $f_{\text{dif}} = 43 \pm 2$  kHz and  $t_{\text{dif}} = 2125$  s. Note that the time-scale was determined with low statistical accuracy, because the observing interval ( $T = 2852$  s) was comparable with the scintillation time. The dynamic spectrum shows narrow frequency details elongated in time.

Frequency and time structure functions are shown in Fig. 8 on a log–log scale. Variations of these functions are presented on the

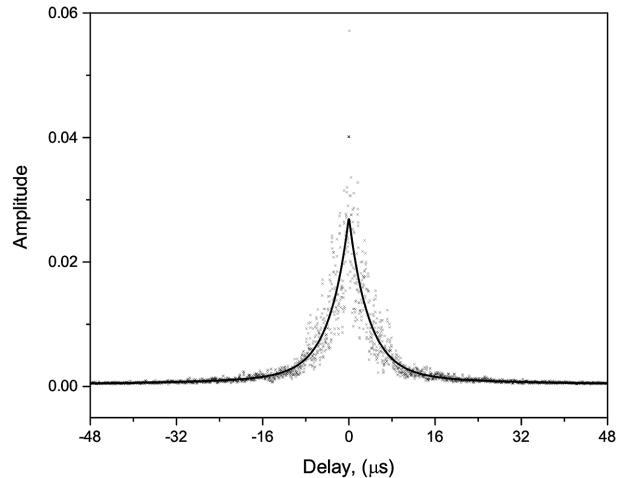


**Figure 9.** PSR B2016+28. Cross-section of visibility function along the delay axis.

same scale, in order to determine the values of the frequency and time-scales at the same level of the structure function. Fitting the value of the structure function at time intervals smaller than the scintillation scale gave the same slope for both structure functions:  $\alpha = 1.05 \pm 0.02$ . Consequently, as shown in Shishov et al. (2003) and Smirnova & Shishov (2008), equal slopes for both functions correspond to the refractive scintillation model. Fig. 9 shows the cross-section of the average visibility function as a function of the delay. Exponential approximation of this cross-section gives the scattering time  $\tau_{\text{sc}} = 2.50 \pm 0.05$   $\mu\text{s}$ . Diffraction stripes in the dynamic spectrum have no observable time drift, which means that the refraction shift is approximately perpendicular to the line-of-sight velocity with respect to the scattering medium.

The spatial scale of the diffraction pattern  $\rho_{\text{dif}}$  in the observer’s plane was obtained from the average covariation function of complex cross-spectra for the space–ground baseline RadioAstron–Arecibo. According to (8), the measured value of the spatial coherence function is  $B_{\text{u}} = 0.26 \pm 0.05$ . Errors were estimated as RMS values at the function tail. Applying (9), one can estimate the scale of the diffraction pattern  $\rho_{\text{dif}} = (3.4 \pm 0.5) \times 10^9$  cm.

The distance to the pulsar and its proper motion were previously measured by Briskin et al. (2002):  $\mu_{\alpha} = -2.6(2)$  mas yr $^{-1}$ ,  $\mu_{\delta} = -6.2 \pm 0.4$  mas yr $^{-1}$ ,  $D = 0.95 \pm 0.09$  kpc. For the pulsar, we have  $V_{\alpha} = -12$  km s $^{-1}$  and  $V_{\delta} = -28$  km s $^{-1}$ . At the date of the observations (MJD = 57164), the velocity of the Earth was  $V_{\alpha,E} = 4.05$  km s $^{-1}$ ,  $V_{\delta,E} = -15.6$  km s $^{-1}$ . Substituting the measured values of  $\rho_{\text{dif}}$  and  $t_{\text{dif}}$  into equation (10), we obtained  $V_{\text{eff}} = 16 \pm 2$  km s $^{-1}$ , where the error is determined by the error in  $\rho_{\text{dif}}$ . This value  $V_{\text{eff}}$  corresponds to a distance to the scattering screen  $d_s/D = 0.01$  (6). The value  $d_s/D = 0.1$  corresponds to the velocity  $V_{\text{eff}} = 19$  km s $^{-1}$ . It is possible to say that  $d_s/D \leq 0.1$ . In these calculations, we did not take into account the velocity of the ISM,  $V_{\text{scr}}$ , which is comparable with  $V_{\text{eff}}$ , so the error in our estimation could be much greater.

The scattering angle in the direction to the pulsar measured from (11) is  $\theta_{\text{sc}} = 0.90 \pm 0.13$  mas or  $\theta_{\text{H}} = 2.1 \pm 0.3$  mas. We have measured a scattering time for this pulsar of  $\tau_{\text{sc}} = 2.5$   $\mu\text{s}$  (Fig. 9).

As previously shown in Shishov et al. (2003), the values of time  $D_s(\Delta t)$  and frequency  $D_s(\Delta f)$  structure functions (see Fig. 8) at a given level provide the refraction angle. A cosmic prism is located in front of the scattering screen, but the distance to the prism  $R_{\text{pr}}$  is

unknown. Thus it is possible to estimate only the upper limit  $R_{\text{pr}} < 0.1D$ . At level 0.2 of the structure function, the time lag is  $t_0 = 303$  s and the frequency lag  $f_0 = 17.2$  kHz. Using equation (40) from Shishov et al. (2003),  $\theta_{\text{ref}} = 3V_{\text{eff}} f t_0 / (R_{\text{pr}} f_0)$ , we obtained a lower limit  $\theta_{\text{ref}} > 23$  mas. Here,  $f = 324$  MHz and  $V_{\text{eff}} = 19$  km s $^{-1}$ . Note that the scattering layer may be located significantly closer to the observer than 100 pc.

## 5 ANALYSIS OF SECONDARY SPECTRA

We have detected parabolic arcs in the secondary spectra for all pulsars except B2016+28. Results of arc curvature  $a$  measurements are presented in Table 4. While calculating the distance to the scattering screens using (5), we neglected the velocities of the screen and the observer. Estimated distances to the screens are also given in Table 4.

Our algorithm for the parabolic arcs approximation goes back to the technique that was described by Bhat et al. (2016), but it has a number of important features. All arclets shown in Fig. 10(c) have the same curvature as the main arc, but the vertices of these arclets are shifted from the origin. The parabola in Fig. 10(h) shows the same behaviour. We parametrized the parabolic arcs by both the curvature parameter  $a$  and the position of the parabola vertex in the frequency lag domain  $\nu_0$ . Also, we used the procedure of binarization. All pixels of the secondary spectrum were converted into ‘0’ or ‘1’ values, depending on the threshold. Varying the threshold, one can obtain many implementations of the secondary spectrum. Some of them will contain only the parabolic features located close to the origin (high threshold level), whereas other values of the threshold show parabolic branches in regions with large delays (low threshold level). Therefore we made multiple measurements of arc parameters and used weighted mean values for further analysis.

The parabola in the secondary spectra of B0823+26 differs slightly from the background level and does not have separate dominant details. The branches can be clearly distinguished only in the region close to the centre of the secondary spectrum (see Fig. 10a and b). Nevertheless, the measurement of the parabola curvature in both experiments led to a similar result. Previously, the curvature of parabolic arcs for this pulsar was measured by Stinebring et al. (2001) at 430 MHz. Reducing these measurements to 324 MHz using relation  $a(f) \propto f^{-2}$  (Hill et al. 2003) gives a curvature value of

$0.25 \mu\text{s MHz}^{-2}$ , which coincides with our estimates. The distance to the screen calculated with (5) is  $0.23 \pm 0.08$  kpc, which also coincides with the measurements outlined above. The distances to the scattering screens obtained from the covariation functions are given in Table 4 ( $d_s^4$ ) and the distance obtained from the secondary spectra analysis is marked as  $d_s^3$  in the table. The distances obtained from the measured  $\tau_{\text{sc}}$  and  $\theta_{\text{H}}$  are shown as  $d_s^5$ .

For B1237+25, the parabolic arcs have a low signal-to-noise ratio. Despite this, extended parabola branches are clearly distinguished (see Fig. 10f and g). The presence of such structures in the secondary spectrum at 430 MHz was noted in Wolszczan & Cordes (1987), but the parabolic arcs themselves were not distinguished. Curvature measurements in both sessions coincide and the distance to the screen turned out to be  $0.23 \pm 0.05$  kpc. It should be noted that this distance is only  $0.28 D$ . Using (14), we can conclude that the size of the scattering disc  $\theta_{\text{H}}$  in these observations was less than 0.8 mas.

Parabolic arcs in the secondary spectrum of B1929+10 can be clearly distinguished above the noise level (see Fig. 10h). Our measurements yield a curvature value of  $0.39 \pm 0.03 \mu\text{s MHz}^{-2}$ . Previously, Hill et al. (2003) performed studies on the curvature estimation at different frequencies. Recalculating their results from 430–324 MHz, we obtained a curvature value of  $0.30 \pm 0.02 \mu\text{s MHz}^{-2}$ , which differs significantly from our result. Putney & Stinebring (2006) showed the presence of at least three different parabolas in the secondary spectrum at 1410 MHz. None of these parabolas recalculated down to our frequency coincides with our measurements. We estimated the distance to the scattering screen to be  $0.61 D$ , which is close to the result obtained in Section 4.3.

The most impressive behaviour of the secondary spectra is observed for B0834+06. In the experiments of 2014 and 2015, parabolic arcs are clearly distinguished (Fig. 10d and f). Moreover, 2015 observations show the arclets that were previously observed by Hill et al. (2003), Cordes et al. (2006) and Briskin et al. (2010). However, in the earlier experiment conducted on 2012 April 26, there was a significant reduction in the diffraction scintillation scales. A large number of individual arcs are observed in the secondary spectrum, which together form a wider parabolic arc. In Fig. 10(c), it is clearly seen that some of the arcs are located simultaneously in a wide range of both positive and negative delays. In addition, for observation 26.04.2012 we have determined the coordinates of the vertices for the most well-distinguished arcs and

**Table 4.** Arc curvature measurements and screen distances.

Pulsar	Obs.code	$D^1$ (kpc)	$\mu_\alpha^2$ (mas yr $^{-1}$ )	$\mu_\delta^2$ (mas yr $^{-1}$ )	$a$ ( $\mu\text{s MHz}^{-2}$ )	$d_s^3$ (kpc)	$d_s^4$ (kpc)	$d_s^5$ (kpc)
B0823+26	RAGS04AJ RAGS04AK	$0.36 \pm 0.08$	$62.6 \pm 2.4$	$-95.3 \pm 2.4$	$0.22 \pm 0.03$ $0.28 \pm 0.02$	$0.24 \pm 0.09$ $0.22 \pm 0.08$	$0.26 \pm 0.03$	$0.17 \pm 0.02$
B0834+06	RAES06C RAGS04AH RAGS04AL	$0.62 \pm 0.06$	$2 \pm 5$	$51 \pm 3$	$0.56 \pm 0.03$ $0.57 \pm 0.03$ $0.58 \pm 0.05$	$0.42 \pm 0.09$ $0.42 \pm 0.09$ $0.42 \pm 0.010$	$0.61 \pm 0.12$	$0.62 \pm 0.06$
B1237+25	RAGS04AP RAGS04AR	$0.85 \pm 0.06$	$-106.82 \pm 0.17$	$49.92 \pm 0.18$	$0.45 \pm 0.05$ $0.42 \pm 0.02$	$0.23 \pm 0.05$ $0.24 \pm 0.03$	$0.40 \pm 0.04$	$\geq 0.22 \pm 0.01$
B1929+10	RAGS04AO	$0.33 \pm 0.010$	$94.08 \pm 0.17$	$43.25 \pm 0.16$	$0.39 \pm 0.03$	$0.19 \pm 0.05$	$0.24 \pm 0.03$	$0.21 \pm 0.01$
B2016+28	RAGS04AQ	$0.95 \pm 0.09$	$-2.6 \pm 0.02$	$-6.2 \pm 0.4$	–	–	$< 0.1$	$0.55 \pm 0.03$

Notes.  $a$  – parabolic arc curvature,  $d_s$  – distance to the scattering screen,  $\mu_\alpha^2, \mu_\delta^2$  – pulsar proper motion

(1) Distances were taken from parallax measurements (Gwinn et al. 1986; Briskin et al. 2002; Liu et al. 2016).

(2) Proper motions were taken from measurements (Gwinn et al. 1986; Lyne et al. 1982; Briskin et al. 2002; Kirsten et al. 2015).

(3) Screen distances estimated by parabolic arcs.

(4) Screen distances estimated using covariation function.

(5) Screen distances estimated using (14).

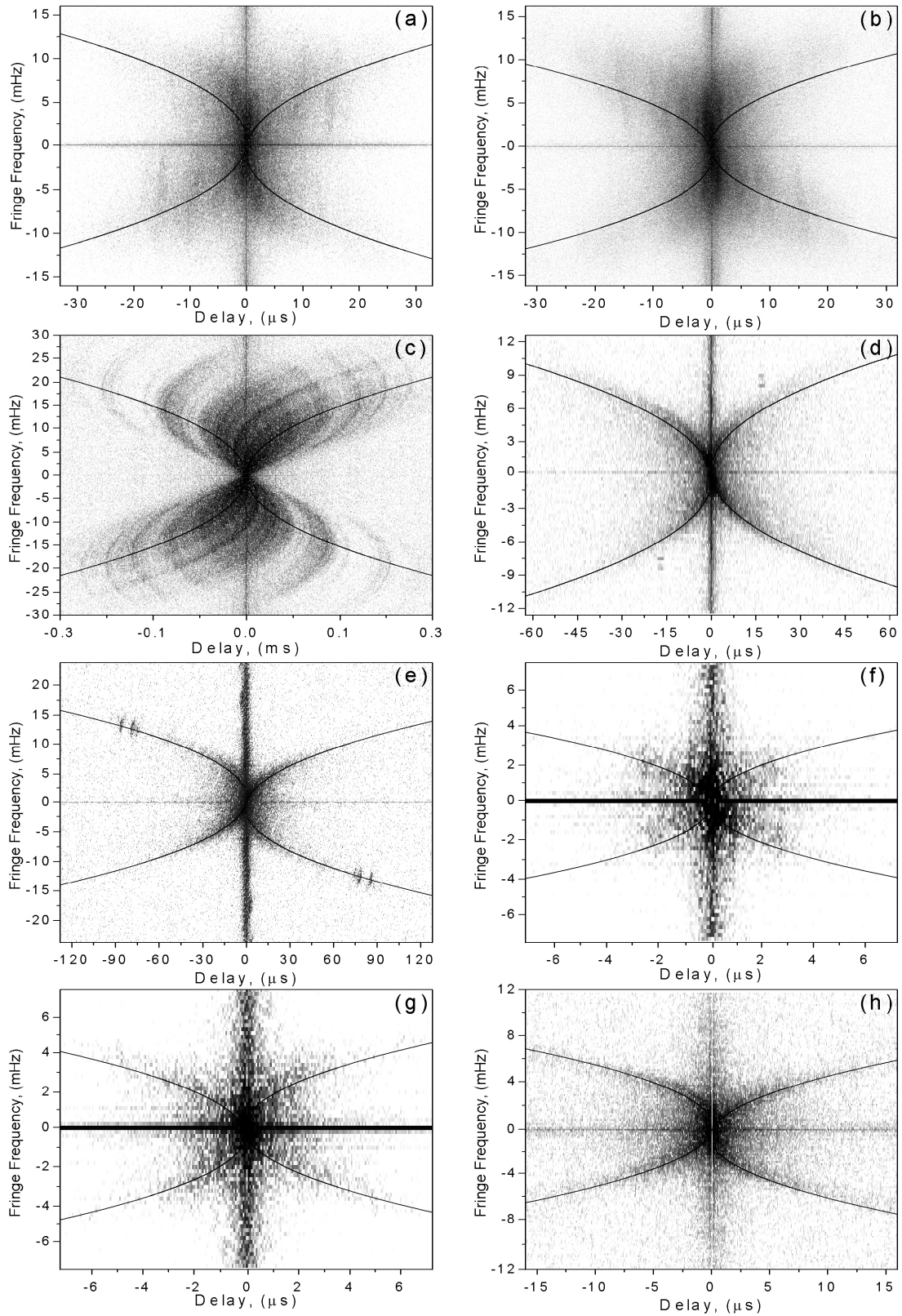


**Figure 10.** Secondary spectra for observed pulsars: (a) B0823+26 (observation RAGS04AJ, 11.03.2015, GBT radio telescope), (b) B0823+26 (observation RAGS04AK, 11.03.2015, GBT radio telescope), (c) B0834+06 (observation RAES06C, 26.04.2012, Arecibo radio telescope), (d) B0834+06 (observation RAGS04AH, 08.12.2014, GBT radio telescope), (e) B0834+06 (observation RAGS04AL, 08.04.2015, Arecibo radio telescope), (f) B1237+25 (observation RAGS04AP, 13.05.2015, GBT radio telescope), (g) B1237+25 (observation RAGS04AR, 07.06.2015, Arecibo radio telescope), (h) B1929+10 (observation RAGS04AO, 05.05.2015, Arecibo radio telescope). Black solid lines correspond to the fitted parabolas for each pulsar.

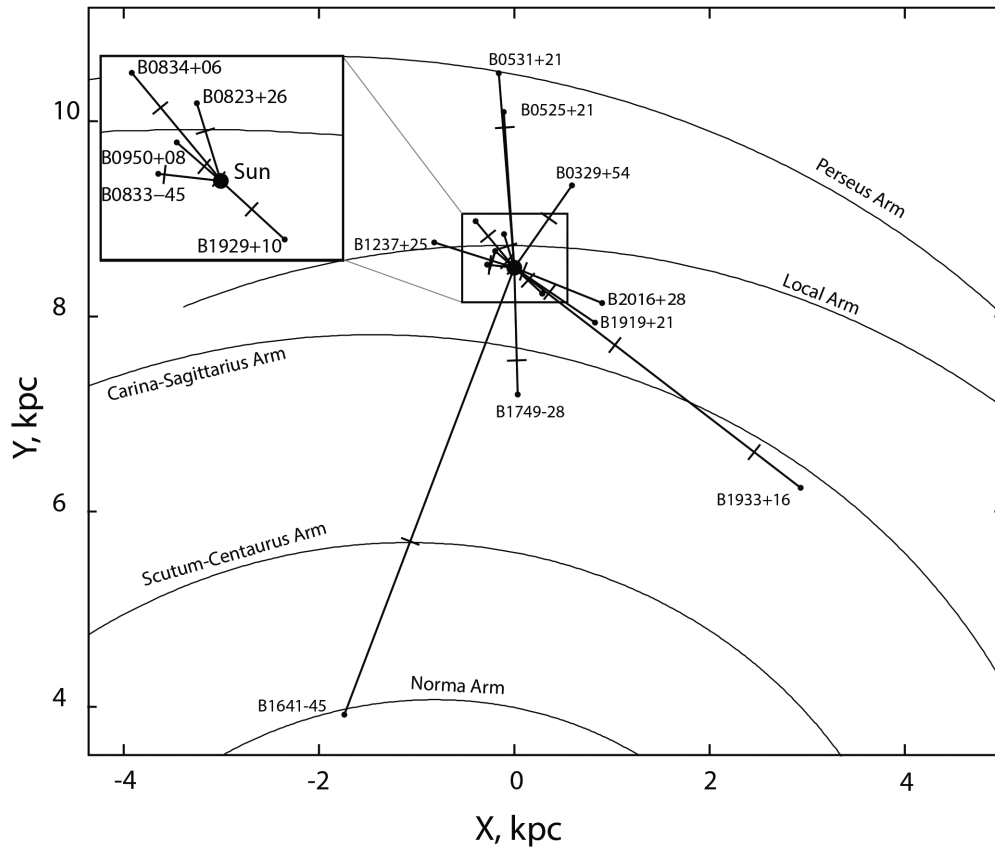


**Figure 11.** Map of pulsars and estimated scattering screens in the Galactic plane.

approximated them. All measurements are in good agreement with the values known from the literature. The distance to the scattering screen calculated from the arcs was equal to  $(0.68 \pm 0.08)D$ , or  $0.42 \pm 0.05$  kpc.

## 6 DISCUSSION

In order to determine the location of the scattering region, we used a thin screen model. This model was proposed right after the discovery of pulsars (Scheuer 1968; Rickett 1977, 1990) and, despite its simplicity, it describes the results of our observations sufficiently well. The uniform model of scattering medium distribution along the line of sight cannot be reconciled with the experimental data for observed pulsars. Therefore, observational evidence favours the conclusion that the scattering is produced mainly by relatively compact plasma layers.

Results of our estimates of distances to effective scattering screens are summarized in Table 4. There is excellent agreement between such estimates made through analysis of parabolic arcs and analysis of measured diffractive scale, scintillation time and pulsar proper motion. A notable discrepancy between these estimates and those made by comparison of scattering time  $\tau$  and scattering angle  $\theta_H$  for several pulsars may be connected with anisotropy of the interstellar inhomogeneities or the presence of multiple screens in the direction to the given pulsars.

The positions of the scattering regions studied in the present and our previous articles (Smirnova et al. 2014; Andrianov et al. 2017; Popov et al. 2016, 2017b; Shishov et al. 2017) are shown by

single dashes in Fig. 11. In some cases (PSR B0823+26, B1641-45, B1749-28, B1933+16), scattering regions were detected near the spiral arms of the Galaxy, where the presence of plasma layers is most probable. For pulsar B1749-28, the scattering screen is located near H II region RCW 142 (G0.55-0.85) and for pulsar B1641-45 the screen can be identified with the H II region G339.1-04 (Popov et al. 2016).

The existence of compact regions with enhanced electron density fluctuations was first inferred from observations of extreme scattering events (ESEs): periods of anomalously strong scattering of radio emission from extragalactic sources (Fiedler et al. 1987). Although ESEs have been studied in many works (Romani, Blandford & Cordes 1987; Fiedler et al. 1994; Rickett, Lyne & Gupta 1997; Walker & Wardle 1998), the origin and physical nature of the objects causing enhanced scattering are still unclear. Recently, it was demonstrated by Vedantham, de Bruyn & Macquart (2017) and Walker et al. (2017) that ESEs in some cases can be linked with the ionized gas that appears as a shell around tiny molecular clumps.

Similar variations in scattering were later also discovered for pulsars (Coles et al. 2015) and these were attributed to turbulent structures in the ISM with sheet-like or rope-like morphology.

Since pulsars are point sources, the interference of scattered rays leads to the formation of parabolic arcs in the secondary spectra. Measuring the parameters of arcs yields information on the location of the scattering plasma and on the structure of the scattering disc (Stinebring et al. 2001; Hill et al. 2003; Walker et al. 2004; Cordes et al. 2006). Thus, observations of pulsars are the most promising source of information on electron density variations in the ISM.

It was shown by Walker et al. (2004), Brisken et al. (2010) and Gwinn et al. (2016) that observed parabolic structures in the secondary spectra may be explained by anisotropic scattering in compact plasma layers. Our results indicate that scintillations are produced in thin regions with an increased level of plasma density fluctuations; these structures responsible for increased scattering are abundant in the ISM.

## 7 CONCLUSION

We have observed five pulsars with the RadioAstron space–ground interferometer at 324 MHz and measured the following scattering parameters: decorrelation bandwidth ( $f_{\text{dif}}$ ), scattering broadening ( $\tau_{\text{sc}}$ ), scintillation time ( $t_{\text{dif}}$ ) and angular size of the scattering disc ( $\theta_{\text{H}}$ ). Distances to the effective scattering screen ( $d_s$ ) were estimated by several techniques using the model of a thin scattering screen. It was shown that the model of uniform inhomogeneities of interstellar plasma along the line of sight to the pulsars is not applicable. The scattering is produced mainly by compact plasma layers. Discrepancies between the values of  $d_s$  determined by different techniques could be explained by anisotropic scattering or by the presence of multiple scattering screens. For PSR0834+06, the scattering parameters measured in 2012 and 2014–2015 differ by more than 50 times. We believe that, for this pulsar, two scattering layers could exist: one is located very close to the pulsar and appears quite rarely, while the other is localized stably for a long time. The arc structure is caused by scattering on this stable screen.

## ACKNOWLEDGEMENTS

The RadioAstron project is led by the Astro Space Center of the Lebedev Physical Institute of the Russian Academy of Sciences and the Lavochkin Scientific and Production Association, under a contract with the State Space Corporation ROSCOSMOS, in collaboration with partner organizations in Russia and other countries.

Partly based on observations with the Green Bank Observatory, which is a facility of the National Science Foundation operated under cooperative agreement by Associated Universities, Inc.

The Arecibo Observatory is operated by SRI International under a cooperative agreement with the National Science Foundation (AST-1100968) and in alliance with Ana G. Mendez-Universidad Metropolitana and the Universities Space Research Association.

This work was supported by the Russian Foundation for Basic Research (project code 16-02-00954).

We are grateful to the reviewer for valuable comments and remarks.

## REFERENCES

Andrianov A. S., Smirnova T. V., Shishov V. I., Gwinn C., Popov M. V., 2017, *Astron. Rep.*, 61, 513  
 Armstrong J. W., Rickett B. J., Spangler S. R., 1995, *ApJ*, 443, 209  
 Bhat N. D. R., Rao A. P., Gupta Y., 1999, *ApJS*, 121, 483

Bhat N. D. R., Ord S. M., Tremblay S. E., McSweeney S. J., Tingay S. J., 2016, *ApJ*, 818, 86  
 Brisken W. F., Benson J. M., Goss W. M., Thorsett S. E., 2002, *ApJ*, 571, 906  
 Brisken W. F., Macquart J.-P., Gao J. J., Rickett B. J., Coles W. A., Deller A. T., Tingay S. J., West C. J., 2010, *ApJ*, 708, 232  
 Britton M. C., Gwinn C. R., Ojeda M. J., 1998, *ApJ*, 501, L101  
 Coles W. A. et al., 2015, *ApJ*, 808, 113  
 Cordes J. M., Rickett B. J., Stinebring D. R., Coles W. A., 2006, *ApJ*, 637, 346  
 Fiedler R. L., Dennison B., Johnston K. J., Hewish A., 1987, *Nature*, 326, 675  
 Fiedler R., Dennison B., Johnston K. J., Waltman E. B., Simon R. S., 1994, *ApJ*, 430, 581  
 Gwinn C. R., Taylor J. H., Weisberg J. M., Rawley L. A., 1986, *AJ*, 91, 338  
 Gwinn C. R., Bartel N., Cordes J. M., 1993, *ApJ*, 410, 673  
 Gwinn C. R., Britton M. C., Reynolds J. E., Jauncey D. L., King E. A., McCulloch P. M., Lovell J. E. J., Preston R. A., 1998, *ApJ*, 505, 928  
 Gwinn C. R. et al., 2016, *ApJ*, 822, 96  
 Hill A. S., Stinebring D. R., Barnor H. A., Berwick D. E., Webber A. B., 2003, *ApJ*, 599, 457  
 Kardashev N. S. et al., 2013, *Astron. Rep.*, 57, 153  
 Kirsten F., Vlemmings W., Campbell R. M., Kramer M., Chatterjee S., 2015, *A&A*, 577, A111  
 Kovalev Y. A. et al., 2014, *Kosmicheskie Issledovaniya*, 52, 430  
 Likhachev S. F., Kostenko V. I., Girin I. A., Andrianov A. S., Rudnitskiy A. G., Zharov V. E., 2017, *J. Astron. Instrum.*, 6, 1750004  
 Liu S., Pen U.-L., Macquart J.-P., Brisken W., Deller A., 2016, *MNRAS*, 458, 1289  
 Lyne A. G., Anderson B., Salter M. J., 1982, *MNRAS*, 201, 503  
 Popov M. V. et al., 2016, *Astron. Rep.*, 60, 792  
 Popov M. V. et al., 2017b, *MNRAS*, 465, 978  
 Putney M. L., Stinebring D. R., 2006, *Chin. J. Astron. Astrophys. Suppl.*, 6, 233  
 Rickett B. J., 1977, *ARA&A*, 15, 479  
 Rickett B. J., 1990, *ARA&A*, 28, 561  
 Rickett B. J., Lyne A. G., Gupta Y., 1997, *MNRAS*, 287, 739  
 Rickett B. J. et al., 2014, *ApJ*, 787, 161  
 Romani R. W., Blandford R. D., Cordes J. M., 1987, *Nature*, 328, 324  
 Scheuer P. A. G., 1968, *Nature*, 218, 920  
 Shishov V. I., Smirnova T. V., 2002, *Astron. Rep.*, 46, 731  
 Shishov V. I. et al., 2003, *A&A*, 404, 557  
 Shishov V. I., Smirnova T. V., Gwinn C. R., Andrianov A. S., Popov M. V., Rudnitskiy A. G., Soglasnov V. A., 2017, *MNRAS*, 468, 3709  
 Smirnova T. V., Shishov V. I., 2008, *Astron. Rep.*, 52, 736  
 Smirnova T. V. et al., 2014, *ApJ*, 786, 115  
 Stinebring D. R., McLaughlin M. A., Cordes J. M., Becker K. M., Goodman J. E. E., Kramer M. A., Sheppard J. L., Smith C. T., 2001, *ApJ*, 549, L97  
 Vedantham H. K., de Bruyn A. G., Macquart J.-P., 2017, *ApJL*, 849, L3  
 Walker M., Wardle M., 1998, *ApJ*, 498, L125  
 Walker M. A., Melrose D. B., Stinebring D. R., Zhang C. M., 2004, *MNRAS*, 354, 43  
 Walker M. A., Tuntsov A. V., Bignall H., Reynolds C., Bannister K. W., Johnston S., Stevens J., Ravi V., 2017, *ApJ*, 843, 15  
 Wolszczan A., Cordes J. M., 1987, *ApJ*, 320, L35

This paper has been typeset from a  $\text{\TeX}/\text{\LaTeX}$  file prepared by the author.